The autophagy protein, ATG14 safeguards against unscheduled pyroptosis activation to enable embryo transport during early pregnancy

Pooja Popli[1], Arin K. Oestreich[2,3], Vineet K. Maurya[4], Marina N. Rowen[2,3], Yong Zhang[5], Michael J. Holtzman[5], Ramya Masand[1], John Lydon[4], Shizuo Akira[6,7], Kelle H. Moley[2,3], and Ramakrishna Kommagani[1,8*]

[1]Department of Pathology and Immunology, Baylor College of Medicine, One Baylor Plaza, Houston, TX 77030, USA

[2]Department Obstetrics and Gynecology,
[3]Center for Reproductive Health Sciences, Washington University School of Medicine, St. Louis, MO, 63110, USA

[4]Department of Molecular and Cellular Biology, Baylor College of Medicine, One Baylor Plaza, Houston, TX 77030, USA

[5]Department of Medicine and Department of Cell Biology, Washington University School of Medicine, St. Louis, MO, 63110, USA

[6]Department of Host Defense, Research Institute for Microbial Diseases (RIMD),
[7]Laboratory of Host Defense, World Premier Institute Immunology Frontier Research Center (WPI-IFReC), Osaka University, Osaka 565-0871, Japan

[8]Department of Molecular Virology and Microbiology, Baylor College of Medicine, One Baylor Plaza, Houston, TX 77030, USA.

***Correspondence to:**

Ramakrishna Kommagani
Associate Professor
Department of Pathology and Immunology
Department of Molecular Virology and Microbiology
Alkek Center for Metagenomics and Microbiome Research
T228A, One Baylor Plaza
Baylor College of Medicine
Houston, TX, 77030
Email: Rama.Kommagani@bcm.edu
Phone: (713)-798-5085
Fax: 713-798-5838

Short title: Cellular self-digestion for female reproductive tract functions

The authors have declared that no conflict of interest exists.

35 **Non-standard Abbreviations**

36 WT: Wild Type

37 HESCs: Human Endometrial stromal cells

38 dpc: Days post coitum

39 E2: Estrogen

40 P4: Progesterone

41 VPS 15: Vacuolar sorting protein 15

42 cKO: Conditional knockout

43 FRT: Female reproductive tract

44 GSDMD: Gasdermin D

45 **Keywords:** fallopian tube, oviduct, embryo transport, uterus, pregnancy failure, infertility

Abstract

Recurrent pregnancy loss (RPL), characterized by two or more failed clinical pregnancies, poses a significant challenge to reproductive health. In addition to embryo quality and endometrial function, proper oviduct function is also essential for successful pregnancy establishment. Therefore, structural abnormalities or inflammation resulting from infection in the oviduct may impede the transport of embryos to the endometrium, thereby increasing the risk of miscarriage. However, our understanding of the biological processes that preserve the oviductal cellular structure and functional integrity is limited. Here, we report that autophagy-related protein ATG14 plays a crucial role in maintaining the cellular integrity of the oviduct by controlling inflammatory responses, thereby supporting efficient embryo transport. Specifically, the conditional depletion of the autophagy-related gene, *Atg14* in the oviduct causes severe structural abnormalities compromising its cellular integrity leading to the abnormal retention of embryos. Interestingly, the selective loss of *Atg14* in oviduct ciliary epithelial cells did not impact female fertility, highlighting the specificity of ATG14 function in distinct cell types within the oviduct. Mechanistically, loss of *Atg14* triggered unscheduled pyroptosis via altering the mitochondrial integrity leading to inappropriate embryo retention and impeded embryo transport in the oviduct. Finally, pharmacological activation of pyroptosis in pregnant mice phenocopied the genetically induced defect and caused impairment in embryo transport. Together, we found that ATG14 safeguards against unscheduled pyroptosis activation to enable embryo transport from the oviduct to uterus for the successful implantation. Of clinical significance, these findings provide possible insights into the underlying mechanism(s) of early pregnancy loss and might aid in developing novel prevention strategies using autophagy modulators.

Introduction

A successful pregnancy is orchestrated by the sequential and coordinated events happening in the FRT [1]. Each of these events is crucial to advance to the next step in pregnancy. For example, as a first step, the ovary undergoes ovulation to release a mature ovum which is collected by oviduct fimbriae and funnelled through the infundibulum into the ampulla where they get fertilized by sperm. The embryos then pass through the ampulla-isthmus junction (AIJ) to enter the isthmus of the oviduct before exiting via the distal utero-tubal junction (UTJ) to implant on the wall of the uterus. Recently, the intricate structural and cellular diversity of the oviduct has drawn significant attention, emphasizing its vital role in facilitating embryo development and transport [2-4]. Morphologically, the oviduct is divided into four evolutionarily conserved regions: the infundibulum (nearest the ovary), ampulla (the site of fertilization), isthmus (serving as a sperm reservoir and site for early embryonic development), and utero-tubal junction (connected to the uterus). Each of these segments comprises epithelial, stromal, and smooth muscle cells with lumen lined up with an epithelium containing secretory ($PAX8^+$) and multi-ciliated ($FOXJ1^+$) cells. While the infundibulum and ampulla are composed of more ciliated than secretory cells, the isthmus has more secretory than ciliated cells [5, 6]. Successful pregnancy requires that the embryo transit the entire oviduct orchestrated by the following: (1) secretory cells producing oviduct fluid, (2) beating cilia to ensure unidirectional flow of the fluid, and (3) periodic contractions of surrounding muscle to propel fluid flow. Therefore, a combination of ciliary and muscular activity contributes to the overall success of oviduct embryo transport. This combination of ciliary and muscular activity plays a crucial role in the effective transport of the embryo through the oviduct. Any perturbations in these early pregnancy events can lead to adverse ripple effects that can compromise pregnancy outcomes. Previous studies have reported that impaired oviductal transport of embryos can lead to pregnancy failure and cause infertility in mice [7-10]. However, the underlying mechanism is not yet completely understood.

96 Autophagy is a cellular process, evolutionarily conserved from yeast to mammals, that
97 recycles long-lived proteins and organelles to maintain cell energy homeostasis. Autophagy
98 is classically activated through the nutrient sensor or mammalian target of the rapamycin
99 complex. Genetic screens for autophagy-defective mutants in yeast and other fungi have
100 currently identified 41 autophagy-related (ATG) genes that play a primary role in autophagy
101 [11, 12]. Approximately half of these genes have homologs in higher organisms, and *Atg14*
102 (also known as Barkor for Beclin 1 (*Becn1*)-associated autophagy-related key regulator) is
103 one of them [13, 14]. ATG14 is part of a protein complex that is composed of Beclin 1, vacuolar
104 sorting protein 15 (VPS15), and VPS34 (also named as Pik3c3, the catalytic subunit of the
105 class III phosphatidylinositol 3-kinase), and this ATG14-containing complex plays an important
106 role in the initiation process of autophagy.

107 Pyroptosis is a type of inflammatory cell death mediated by gasdermin (GSDM) and is
108 a product of continuous cell expansion until the cytomembrane ruptures, resulting in the
109 release of cellular contents that can activate strong inflammatory and immune responses.
110 Gasdermin family proteins are the primary executioners of pyroptosis. Cytotoxic N-terminal of
111 gasdermins generated from caspases mediated cleavage of gasdermin proteins oligomerizes
112 and forms pores across the cell membrane, leading to the release of proinflammatory
113 cytokines such as interleukin-1β (IL-1β) and interleukin-18 (IL-18). Aberrant activation of
114 pyroptosis has been implicated in the progression of many diseases including cancer and
115 autoimmune, cardiovascular, and infectious diseases [15-17]. Recent studies have shown that
116 the interactions between pyroptosis and autophagy play an important role in various
117 physiological and pathological processes [15-20]. For example, autophagy inhibition
118 upregulates galangin-induced pyroptosis in human glioblastoma multiforme cells and
119 promotes pneumococcus-induced pyroptosis [21, 22]. However, the studies defining the
120 molecular interactions between the pyroptosis, and autophagy pathways are very limited.

121 With a better understanding of the fundamental process of autophagy, its
122 pathophysiological functions have begun to be appreciated in the female reproductive tract.

123 For example, mice deficient in key autophagy genes such as genetic knockout of *Atg7* or
124 *Becn1* result in primary ovarian insufficiency and reduced progesterone production [23, 24].
125 Similarly, recent studies from our group established the roles of three different autophagy-
126 specific genes: *Atg16l*, *Fip200*/*Rb1cc1*, or *Becn1* in endometrial physiological processes,
127 including receptivity and decidualization [25-27]. However, none of these genes exhibited any
128 discernible impact on oviduct function. Surprisingly, in this study, we revealed a critical role for
129 ATG14 in maintaining proper oviduct function, specifically enabling the transport of embryos
130 to the uterus- a function distinct from that of other autophagy-related proteins. Loss of ATG14
131 in the oviduct resulted in severe structural abnormalities, compromising its cellular integrity,
132 and ultimately leading to embryo retention and infertility.

133 **Materials and Methods**

134 **Animal care and use:**

135 All animal studies were approved by the Institutional Animal Care and Use Committee of
136 Washington University School of Medicine, Saint Louis, MO, USA, and the Use Committee of
137 Baylor College of Medicine, Houston, TX, USA. *Atg14* f/f mice were provided by a gift from Dr.
138 Shizuo Akira at the Department of Host Defense, Research Institute for Microbial Diseases
139 (RIMD), Osaka University, and previously described [28]. Wild-type Pr-cre mice were provided
140 by Dr. John Lydon at Baylor College of Medicine, Houston, and previously described [29].
141 $Atg14^{flox/flox}$ mice, in which exon 4 was flanked by loxp sites, were bred to progesterone
142 receptor cre ($PR^{cre/+}$) mice to generate ($Atg14^{flox/flox}$; $PR^{cre/+}$ mice), hereafter referred to as *Atg14*
143 cKO mice. Both control and conditional knockout females were generated by crossing females
144 carrying homozygous $Atg14^{flox/flox}$ alleles with *Atg14* cKO males. *Foxj1-cre* mice were a
145 generous gift from Dr. Michael J. Holtzman at Washington University St. Louis and previously
146 described [30]. *Foxj1*/*Atg14* cKO mice were generated by crossing females carrying
147 homozygous $Atg14^{f/f}$/$Foxj1^{f/f}$ females with $Atg14^{f/f}$/*Foxj1-cre* males. All mice were age-
148 matched and on a C57BL/6 genetic background (The Jackson Laboratory, Bar Harbor, ME).
149 Mice were genotyped by PCR analysis of genomic DNA isolated from tail clippings using the
150 gene-specific primers listed in **Supplementary Table 1.**

151 **Fertility analysis and timed mating**

152 Female fertility was determined by mating cohorts of *Atg14* cKO experimental (n=6) and
153 control *Atg14* f/f (n=4) females individually starting at 8 weeks of age with sexually mature
154 males of proven fertility. Similarly, breeding trials were set up for *Foxj1/Atg14*-cre females
155 (n=6) and *Foxj1*/*Atg14* control 8-week-old f/f females (n=6). The numbers of litters and pups
156 were tracked over 6 months for each female. Pups per litter for each genotype are reported
157 as mean ± SEM. For timed mating, the morning on which the copulatory plug was first
158 observed was considered 1 dpc. To visualize implantation sites, mice received a tail vein

159 injection of 50 μL of 1% Chicago Sky Blue dye (Sigma-Aldrich, St. Louis, MO, USA) at 5 dpc
160 just before sacrifice.

161 **Steroid hormone treatments**

162 The hormonal profile of pregnancy at the time of implantation was done using a previously
163 described experimental scheme [26]. Briefly, *Atg14* cKO and control females (8 weeks old)
164 were bilaterally ovariectomized under ketamine anesthesia with buprenorphine-SR as an
165 analgesic. Mice were allowed to rest for two weeks to dissipate all endogenous ovarian
166 hormones. After the resting period, mice were injected with 100 ng of estrogen (E2; Sigma-
167 Aldrich) dissolved in 100 μL of sesame oil on two consecutive days and then allowed to rest
168 for two days. At this point, mice were randomly divided into three groups of five: Vehicle-
169 treated (E2 priming) mice received four consecutive days of sesame oil injections; E2 group
170 mice received three days of sesame oil injections followed by a single injection of 50 ng of E2
171 on the fourth day; The E2/P4 mice received 1 mg of progesterone (P4; Sigma-Aldrich) for
172 three consecutive days followed by a single injection of 1 mg P4 plus 50 ng E2 on the fourth
173 day. All hormones were delivered by subcutaneous injection in a 90:10 ratio of sesame oil:
174 ethanol. Mice were euthanized 16 hours after the final hormone injection to collect the uteri. A
175 small piece of tissue from one uterine horn was processed in 4% neutral buffered
176 paraformaldehyde for histology, and the remaining tissue was snap-frozen and stored at -80
177 °C.

178 **Hormone Analysis**

179 For serum hormone level measurement, blood was collected from D4 pregnant mice before
180 mice were sacrificed. Serum was separated from the blood by centrifugation and stored at -
181 80°C before hormone analysis. Serum P4 and E2 levels were measured by using ELISA kits
182 (Enzo Life Sciences) according to the manufacturer's instructions.

183 **Hematoxylin and eosin staining**

184 Tissues were fixed in 4% paraformaldehyde, embedded in paraffin, and then sectioned (5 μm)
185 with a microtome (Leica Biosystem, Wetzlar, Germany). Tissue sections were deparaffinized,
186 rehydrated, and stained with Hematoxylin and Eosin (H&E) as described previously [31]. All
187 the histology was performed on three sections from each tissue of individual mice, and one
188 representative section image is shown in the respective figures.

189 **Histological analysis**

190 For histological analysis, the collected tissues (oviduct or uteri) were fixed in 4%
191 paraformaldehyde, embedded in paraffin, and sectioned. Sections (5 μm) were
192 immunostained (n=5 per group) as described previously [31]. Briefly, after deparaffinization,
193 sections were rehydrated in an ethanol gradient and then boiled for 20 min. in citrate buffer
194 (Vector Laboratories Inc., Newark, CA, USA) for antigen retrieval. Endogenous peroxidase
195 activity was quenched with Bloxall (Vector Laboratories Inc.), and tissues were blocked with
196 2.5% goat serum in PBS for 1 hr (Vector Laboratories Inc.). After washing in PBS three times,
197 tissue sections were incubated overnight at 4 °C in 2.5% goat serum containing the primary
198 antibodies listed in **Supplementary Table 2.** Sections were incubated for 1 hr with biotinylated
199 secondary antibody, washed, and incubated for 45 min with ABC reagent (Vector Laboratories
200 Inc.). Color was developed with 3, 3'-diaminobenzidine (DAB) peroxidase substrate (Vector
201 Laboratories Inc.), and sections were counter-stained with hematoxylin. Finally, sections were
202 dehydrated and mounted in Permount histological mounting medium (Thermo Fisher
203 Scientific, Waltham, MA, USA).

204 **Transmission electron microscopy (TEM)**

205 For ultrastructural analysis, oviducts were fixed in 2% paraformaldehyde/2.5% glutaraldehyde
206 (Ted Pella Inc., Redding, CA) in 100 mM cacodylate buffer, pH 7.2 for 1 hr at room temperature
207 and then overnight at 4°C. Samples were washed in cacodylate buffer and postfixed in 1%
208 osmium tetroxide (Ted Pella Inc.) for 1 hr. Samples were then rinsed extensively in dH20 prior
209 to en bloc staining with 1% aqueous uranyl acetate (Ted Pella Inc.) for 1 hr. Following several
210 rinses in dH20, samples were dehydrated in a graded series of ethanol and embedded in

211 Eponate 12 resin (Ted Pella Inc.). For initial evaluation semithin sections (0.5 μm) were cut
212 with a Leica Ultracut UCT7 ultramicrotome (Leica Microsystems Inc., Bannockburn, IL) and
213 stained with toluidine blue. Sections of 95 nm were then cut and stained with uranyl acetate
214 and lead citrate and viewed on a JEOL 1200 EX II transmission electron microscope (JEOL
215 USA Inc., Peabody, MA). Images at magnifications of 3,000X to 30,000X were taken with an
216 AMT 8-megapixel digital camera (Advanced Microscopy Techniques, Woburn, MA).

217 **Immunofluorescence analysis**

218 Formalin-fixed and paraffin-embedded sections were deparaffinized in xylene, rehydrated in
219 an ethanol gradient, and boiled in a citrate buffer (Vector Laboratories Inc.) for antigen
220 retrieval. After blocking with 2.5% goat serum in PBS (Vector laboratories) for 1 hr at room
221 temperature, sections were incubated overnight at 4°C with primary antibodies
222 (**Supplementary Table 2**) diluted in 2.5% normal goat serum. After washing with PBS,
223 sections were incubated with Alexa Fluor 488-conjugated secondary antibodies (Life
224 Technologies, Carlsbad, CA, USA) for 1 hr at room temperature, washed, and mounted with
225 ProLong Gold Antifade Mountant with DAPI (Thermo Fisher Scientific). All
226 Immunofluorescence images were obtained using a Zeiss LSM 880 confocal microscope (10x
227 and 40x objective lens).

228 Fresh oviduct tissues from 8-week-old mice from control (n=3) and cKO (n=3) were
229 collected and fixed in 4 % PFA at 4ºC overnight. After that, oviducts were washed with PBS
230 and cryoprotected using gradually increased sucrose concentrations in a row (15 and 30%
231 w/v). 24 h later, oviducts were embedded in an OCT medium, frozen (−80 °C), and cryo-
232 sectioned in the CM3050S Cryostat (Leica Biosystems, Germany). The cryosections were
233 mounted on Superfrost plus glass slides (Fisher Scientific, Pittsburgh, PA) and stored at −80°C
234 until used.

235 Cryo-sections were processed for immunofluorescence staining as described before
236 [32]. Briefly, cryosections were blocked in 2.5% normal goat serum. After washing with PBS,

237 sections were blocked with Mouse on Mouse (M.O.M.) IgG blocking reagent (M.O.M.
238 Fluorescein Kit, Vector Laboratories, #FMK-2201) diluted in 1% BSA per the manufacturer's
239 instructions. After blocking, sections were incubated overnight at 4°C with primary antibodies
240 (**Supplementary Table 2**) diluted in 2.5% normal goat serum. Next day, following washing
241 with PBS, sections were incubated with Alexa Fluor 488-conjugated secondary antibodies
242 (Life Technologies, Carlsbad, CA, USA) for 1 hr at room temperature, washed, and mounted
243 with ProLong Gold Antifade Mountant with DAPI (Thermo Fisher Scientific). All
244 Immunofluorescence images were imaged using a Nikon Fluorescent microscope.

245 **Western blotting**

246 Protein lysates (40 µg per lane) from uteri or oviducts were loaded on a 4-15% SDS-PAGE
247 gel (Bio-Rad, Hercules, CA, USA), separated in 1X Tris-Glycine Buffer (Bio-Rad), and
248 transferred to PVDF membranes via a wet electro-blotting system (Bio-Rad), all according to
249 the manufacturer's directions [33]. PVDF membranes were blocked for 1 hour in 5% non-fat
250 milk in Tris-buffered saline containing 0.1% Tween-20 (TBS-T, Bio-Rad), then incubated
251 overnight at 4 °C with antibodies listed in **Supplementary Table 2** in 5% BSA in TBS-T. Blots
252 were then probed with anti-Rabbit IgG conjugated with horseradish peroxidase (1:5000, Cell
253 Signaling Technology, Danvers, MA, USA) in 5% BSA in TBS-T for 1 hr at room temperature.
254 Signal was detected with the Pierce™ ECL Western Blotting Substrate (Millipore, Billerica,
255 MA, USA), and blot images were collected with a Bio-Rad ChemiDoc imaging system.

256 **RNA Isolation and Quantitative Real-Time RT-PCR Analysis**

257 Tissues/cells were lysed in RNA lysis buffer, and total RNA was extracted with the Purelink
258 RNA mini kit (Invitrogen, Carlsbad, CA, USA) according to the manufacturer's instructions.
259 RNA was quantified with a Nano-Drop 2000 (Thermo Fisher Scientific). Then, 1 µg of RNA
260 was reverse transcribed with the High-Capacity cDNA Reverse Transcription Kit (Thermo
261 Fisher Scientific). The amplified cDNA was diluted to 10 ng/µL, and qRT-PCR was performed
262 with primers listed in the **Supplementary Table 1** and TaqMan 2X master mix (Applied
263 Biosystems/Life Technologies, Grand Island, NY, USA) on a 7500 Fast Real-time PCR system

264 (Applied Biosystems/Life Technologies). The delta-delta cycle threshold method was used to
265 normalize expression to the reference gene 18S.

266 **Treatment of mice with Polyphyllin VI**

267 Polyphyllin VI (Selleck chemicals, Houston, TX, USA), a pharmacological agent that induces
268 caspase-1-mediated pyroptosis, was used to study its effects on embryo transport in the
269 oviduct [34]. Eight-week-old C57BL/6 mice were injected for three consecutive days starting
270 from 1 dpc with Polyphyllin VI activator dissolved in 40% PEG-300 (15mg/kg body weight).
271 Dimethyl sulfoxide with 40% PEG-300 was administered as a vehicle.

272 **Statistics**

273 A two-tailed paired student t-test was used to analyze data from experiments with two
274 experimental groups and one-way ANOVA followed by Tukey's post hoc multiple range test
275 was used for multiple comparisons. All data are presented as mean ±SEM. GraphPad Prism
276 9 software was used for all statistical analyses. Statistical tests, including p values, are
277 reported in the corresponding figure legends or, when possible, directly on the data image. To
278 ensure the reproducibility of our findings, experiments were replicated in a minimum of three
279 independent samples, to demonstrate biological significance, and at least three independent
280 times to ensure technical and experimental rigor and reproducibility.
281

282 **Results**

283 **Conditional deletion of *Atg14* in the FRT results in infertility despite the normal ovarian**
284 **function**

285 To explore the role of *Atg14* in uterine function, we first determined its expression
286 levels in the uterus during early pregnancy (Day 1-7) in mice. We found distinct expression of
287 ATG14 in all the uterine compartments (luminal epithelium, glands, and stroma) by day 1 of
288 pregnancy, which disappeared by day 2 of pregnancy (**Fig. 1A**). However, the ATG14
289 expression in the uterus reappeared by day 3 and persisted through the day 7 of pregnancy.
290 The period from day 3 to day 7 is critical, as it is during this time when the uterus begins to
291 prepare for embryo implantation and undergoes the decidualization process. Consistent with
292 protein expression, similar *Atg14* expression at mRNA levels was noted in uteri from early
293 pregnant mice (**Fig. 1B**). This analysis suggests a potential role for ATG14 protein in the
294 uterine physiologic adaptations during early pregnancy. Thus, to study the role of ATG14 in
295 uterine function, we generated a conditional knockout ($PR^{cre/+}$ /$Atg14^{flox/flox}$) mouse model by
296 crossing *Atg14* flox/flox mice with mice expressing Cre recombinase under the control of
297 progesterone receptor promoter ($PR^{cre/+}$). Histological examination of the uterus from adult
298 females showed no gross morphological differences between *Atg14* cKO and control mice
299 (**Fig. S1A**). Further, we did not find any overt defects in the ovary as cKO mice had normal
300 follicles and corpus luteum like their corresponding controls (**Fig. S1B**). Analysis of transcript
301 levels from the uterus, ovary, and liver showed that while *Atg14* levels were efficiently depleted
302 in uteri from cKO mice the levels were unaltered in the ovary and liver samples in control and
303 cKO mice (**Fig. 1C**). Immunofluorescence analysis further confirmed the efficient deletion of
304 ATG14 in all uterine compartments (epithelium and stroma) of cKO mice uteri compared to
305 corresponding control groups (**Fig. 1D**).

306 Considering the effective ablation, a 6-month breeding study was performed mating
307 virile wild-type male mice with adult *Atg14* cKO and control female mice. We found that *Atg14*
308 cKO females did not deliver any litter during the 6-months trial period. However, the control
309 female (*Atg14* flox/flox) mice delivered an average of ~7-8 pups per litter every month (**Table**

310 **1**) (**Fig. 1E**). These findings suggest an indispensable role of *Atg14* in female fertility with intact
311 ovarian function.

312 **Loss of *Atg14* results in impaired embryo implantation and uterine receptivity in mice**

313 Based on the normal ovarian morphology, we posited that the infertility observed in
314 females with *Atg14* cKO status could be attributed to compromised uterine functioning.
315 Analysis of the implanting embryos at Day 5 of pregnancy showed no implantation sites in the
316 uteri of *Atg14* cKO females, whereas ~8 to 9 implantation sites were seen in the uteri of control
317 mice at 5 dpc (**Fig. 2A, left panel**). Whilst there was no embryo present in the uterine lumen
318 of *Atg14* cKO mice, a fully attached embryo encapsulated by the luminal uterine epithelium,
319 was seen in control mice uteri (**Fig. 2A, middle panel**). Additionally, MUC1, a receptive
320 marker expression persisted in the luminal epithelium of cKO mice uteri at 5 dpc as well as 4
321 dpc (**Fig. 2A, right panel, Fig. 2C**). The process of successful embryo attachment and
322 implantation within the uterus necessitates a transition from a non-receptive to a receptive
323 state, a transformation orchestrated under the regulated influence of steroid hormones. Thus,
324 the effects of *Atg14* loss on uterine responsiveness to steroid hormones E2 and P4 were
325 characterized. We performed an established hormone-induced uterine receptivity experiment,
326 which involved ordered and co-stimulatory actions of E2 and P4 leading to the initiation of a
327 receptive phase [35]. In response to E2 treatment, uteri from both *Atg14* control and cKO mice
328 showed similar proliferation as evidenced by Ki-67 staining (**Fig. 2B, middle panel**). Following
329 the co-stimulation with E2+P4 treatment, epithelial proliferation was inhibited with concomitant
330 induction of stromal cell proliferation in control mice uteri indicating fully receptive uteri (**Fig.
331 2B**). Interestingly, cKO mice uteri failed to elicit sub-epithelial stromal cell proliferation and
332 showed intact P4-driven inhibition of epithelial proliferation. Consistently, uteri from *Atg14* cKO
333 mice at 4 dpc showed a reduced number of proliferating stromal cells (**Fig. 2D**). The absence
334 of significant changes in E2-induced targets, such as *Lif*, *Mcm2*, *Ccnd1*, and *Fgf18*, at 4 dpc
335 (**Fig. 2E**) supports our conclusion that ATG14 is required for P4-mediated but not for E2-
336 mediated actions during uterine receptivity. Moreover, the normal serum levels of E2 and P4

337 at D4 of pregnancy rule out any hormonal imbalances, strongly suggesting that the observed
338 phenotype is primarily due to the uterine-specific loss of *Atg14* (**Fig. 2F**).

339 ***Atg14* is required for maintaining oviductal cell structural integrity and embryo**
340 **transport**

341 Given that *Atg14* cKO mice had impaired embryo implantation, we wondered whether
342 embryos are reaching the uterus timely through the oviduct. To determine this, we flushed
343 embryos from both the control and cKO mice uteri on day 4 of pregnancy. Interestingly, in cKO
344 mice, we could retrieve only 1-2% of embryos from their uteri, whereas in control mice, 100%
345 of well-developed blastocysts were retrieved from their uteri (**Fig. 3A & B**). To ensure the
346 timely transport of all embryos from the oviducts to the uteri, we also flushed oviducts from
347 both control and cKO mice. As expected, in the control mice oviduct flushing, we could not
348 recover any embryos or blastocysts, indicating their precise and timely transport to the uterus.
349 Unexpectedly, oviduct flushing from cKO mice resulted in the retrieval of approximately 90%
350 of embryos, suggesting their potential entrapment within the oviducts, impeding their transit to
351 the uterus (**Fig. 3A & B)**. At 4 dpc, there was no significant difference in the average number
352 of blastocysts, morula, or non-viable or retrieved from *Atg14* control uteri and cKO oviducts
353 (**Fig. S4A**)**.** However, we noted that the percentage of developmentally delayed embryos
354 appeared to be higher in *Atg14* cKO oviducts compared to the embryos retrieved from control
355 uteri (**Fig. 3C**). The histological analysis further confirmed an entrapped embryo in the ampulla
356 of *Atg14* cKO at 4 dpc as shown in **Fig. 3D**. Given the embryo retention phenotype in oviduct,
357 we sought to determine if ATG14 is expressed in this region. Consistent with previous studies
358 reporting PR-cre activity in the isthmus [8, 29], we found a significant depletion of ATG14 in
359 the isthmus compared to the ampulla (**Fig. S2A**). Further, the increased p62 and LC3B
360 expression in cKO oviducts suggests that the observed embryo retention phenotype might be
361 attributed to the loss of ATG14-dependent autophagy in cKO oviducts (**Fig. S2B**).

362 Similarly, when we super-ovulated the mice and looked for the embryos on day 4 of
363 pregnancy, we could recover ~20-25 embryos from the cKO mice oviducts compared to only

364 4-5 embryos that were able to reach the uterus. In comparison, in control mice, 90% of
365 embryos were able to complete their pre-destined and timely transport to the uterus (**Fig. 3E**),
366 except 1-2% of unfertilized embryos, which remained in their oviducts.

367 To understand the underlying cause for retained embryos in cKO mice oviducts, we
368 performed histology analysis and determined the structural morphology of their oviducts. The
369 cKO mice oviduct lining shows marked eosinophilic cytoplasmic change akin to
370 decidualization in human oviducts. Some of the cells showed degenerative changes with
371 cytoplasmic vacuolization and nuclear pyknosis, loss of nuclear polarity, and loss of distinct
372 cell borders giving an appearance of fusion of cells (**Fig. 3F**). The marked cytologic
373 enlargement appears to cause luminal obliteration or narrowing resulting in a completely
374 unorganized, obstructed, and narrow lumen, thereby, hampering the path of embryos to reach
375 the uterus as evident from an entrapped embryo shown in **Fig. 3D**. Further, epithelial
376 (cytokeratin KRT8-positive) and myosalpinx (α-smooth muscle active [SMA]-positive,) marker
377 analysis revealed completely distorted epithelial structures (in terms of loss of epithelial cell
378 integrity) with no overt defects in the muscle organization in oviducts of cKO mice (**Fig. 3F,**
379 **lower panel**). Notably, the ampullary region from cKO oviducts seems to be normal with intact
380 epithelial and smooth muscle structures as evident from KRT8 and SMA staining (**Fig. 3F,**
381 **upper panel**).

382 **Selective loss of *Atg14* in oviduct cilia is dispensable for female fertility**

383 The oviduct epithelium primarily consists of two types of cells: ciliated and secretory
384 (non-ciliated) cells. Ciliated cells play a role in embryo and oocyte transport by means of ciliary
385 beat, and non-ciliated/secretory cells produce an oviductal fluid that is rich in amino acids and
386 various molecules, thereby providing an optimal micro-environment for sperm capacitation,
387 fertilization, embryonic survival, and development [36]. Therefore, we determined whether
388 oviducts from cKO mice possess normal ciliated and secretory cell composition. To do so, we
389 examined the expression of various markers, including acetylated-α-tubulin (cilia marker),
390 FOXJ1 (ciliogenesis markers), and PAX8 (non-ciliated/ secretory cell marker) in control and

391 cKO oviducts. As shown in **Fig. 4A**, normal ciliary structures were observed in the ampulla of
392 both control and cKO oviducts. However, in the isthmus of cKO oviducts, we observed a
393 reduction in both FOXJ1- and PAX8-expressing cells **(Fig. 4B**, and **Fig. S3**). Given the
394 importance of cilia in embryo transport, we wondered whether the loss of *Atg14* in oviduct cilia
395 has any impact on embryo transport. To address this, we generated a *Foxj1*-cre/+; *Atg14* f/f
396 mouse model, wherein *Atg14* will be ablated only in ciliary epithelial cells. We observed that
397 ciliated epithelial cells that were positive for acetylated α-tubulin staining did not appear to be
398 different in Foxj1$^{Cre/+;}$ *Atg14* f/f mice oviduct compared to controls suggesting normal
399 ciliogenesis in Foxj1$^{Cre/+}$; *Atg14* f/f mice (**Fig. 4C**).

400 The 6-month breeding trial revealed that loss of *Atg14* in oviductal cilia had no impact
401 on fertility (**Table 2**, **Fig. 4D & E**). Consistently, D5 implantation study analysis showed ~7-8
402 visible embryo implantation sites in *Foxj1/Atg14* cKO mice like their corresponding controls
403 suggesting that embryos were able to make their way to the uterus in a timely manner and
404 undergo implantation despite the ablation of *Atg14* in the oviduct ciliary epithelial cells (**Fig.
405 4F**). These findings suggest that ciliary expression of *Atg14* is dispensable for embryo
406 transport.

407 **ATG14 maintains mitochondria integrity and prevents unscheduled pyroptosis
408 activation in the oviduct to enable embryo transport**

409 To gain more insights into structural defects, we performed TEM analysis on oviducts
410 collected from both control and cKO females on day 4 of pregnancy. Interestingly, oviducts
411 from cKO females had numerous altered mitochondrial structures with abnormally enlarged
412 mitochondria and a less dense matrix compared to control oviducts that had small and
413 compact mitochondria with tight cristae and a dense matrix (**Fig. 5A**). Corroborating and
414 extending those findings, we observed marked reductions of mitochondria network (as defined
415 by TOM20 staining) in the sub-nuclear region of oviducts from *Atg14* cKO mice compared to
416 more densely packed mitochondrial network in the sub-nuclear region of control ones (**Fig.
417 5B**). Further co-localization study analysis revealed a uniform co-localization of Cytochrome

418 C with the TOM20 positive mitochondrial network in control oviducts reflecting the intact
419 mitochondrial integrity (**Fig. 5B**). In contrast, in *Atg14* cKO oviducts, cells with disrupted
420 mitochondrial networks exhibited increased cytosolic leakage of Cytochrome C (**Fig. 5B**).
421 Additionally, analysis of various mitochondrial functional and architecture markers (*Cox4i2*,
422 *Pink1*, *Opa1,* and *Drp1* showed reduced expression in *Atg14* cKO compared to controls (**Fig.**
423 **5C**).

424 Having identified the cellular mechanisms of Atg14, we aimed to delineate the
425 underlying molecular mechanisms associated with Atg14 function in the oviduct. Since we
426 found mitochondrial defects with ATG14 loss and altered mitochondrial structures have been
427 linked to the activation of pyroptosis, we determined if ATG14 regulates pyroptosis in
428 the oviduct [37-39]. First, we assessed the key primary executors of the pyroptosis pathway,
429 Gasdermin D (GSDMD), and caspase-1. Immunofluorescence analysis revealed a remarkable
430 upregulation in GSDMD and caspase-1 expression in the cKO oviducts compared to controls
431 (**Fig. 5D & E**). However, histological analysis of uterus and ovary showed no induction in
432 GSDMD expression compared to their corresponding controls (**Fig. 5F**). Western blot analysis
433 further confirmed elevated expression of caspase-1 and GSDMD in cKO oviducts in
434 comparison to control oviducts as shown in **Fig. 5G.** Additionally, the qPCR analysis
435 demonstrated elevated levels of inflammatory markers, such as *Tnf-α* and *Cxcr3* in cKO
436 oviducts compared to control ones (**Fig. 5H**). Based on these findings, we posit that Atg14
437 plays a crucial role in regulating the pyroptotic pathway by preserving the mitochondrial
438 structural and functional integrity in the oviduct.

439 To substantiate the notion, we also evaluated the impact of unscheduled activation of
440 pyroptosis on embryo transport. To test this, we employed a pyroptosis inducer, Polyphyllin
441 VI, and chose the optimal dose based on the established studies [34]. Wild-type females were
442 mated with virile males and following the plug detection treated with Polyphyllin VI for three
443 consecutive days from 1 to 4 dpc (**Fig. 6A**). We chose to treat mice from 1 to 4 dpc to activate
444 unwarranted pyroptosis in oviduct during the embryo transport. Following the treatments, the

445 oviducts, and uteri from both vehicle-treated and Polyphyllin VI-treated were flushed. We
446 found that pregnant females treated with Polyphyllin VI showed ~50% embryo retention in the
447 oviduct, whereas in the vehicle-treated group, no embryos were retained in the oviduct (**Fig.**
448 **6A-C**). Further analysis of embryos retrieved from Polyphyllin-treated oviducts showed more
449 percentage of developmentally delayed and non-viable embryos compared to embryos
450 recovered from control uteri (**Fig. 6D**). The average number of embryos recovered from
451 polyphyllin- and vehicle-treated mice was not significantly different (**Fig. S4B**). Histological
452 analysis showed a marked induction in GSDMD expression compared to vehicle-treated mice
453 oviducts (**Fig. 6E**). However, precisely activating the unscheduled pyroptosis during the critical
454 period of embryo transport is technically challenging. Nonetheless, our findings provide
455 evidence that unscheduled pyroptosis adversely affects embryo transport through the oviduct.
456 Taken together, these results demonstrate that *Atg14* safeguards pyroptosis activation in the
457 oviduct and allows the smooth transport of embryos to the uterus (**Fig. 6F**).

458 **Discussion**

459 In this study, we delineated the essential role of ATG14 in maintaining the structural
460 integrity of the oviduct by preventing pyroptosis, which enables smooth embryo transit during
461 early pregnancy. Specifically, we dissected the tissue-specific functions of ATG14 in the FRT
462 using Cre driver mice targeting the female reproductive tract. Given that PR-Cre expresses
463 postnatally in different tissues of FRT such as corpus luteum, oviducts, and different cellular
464 compartments (epithelial, stromal, and myometrium) of uteri [29], we found that conditional
465 ablation of ATG14-mediated functions in FRT resulted in infertility owing to hampered
466 transport of embryos from the oviduct. Additionally, *Atg14* loss in uteri causes impaired embryo
467 implantation and receptivity. Its ablation in the oviduct might lead to the activation of
468 pyroptosis, an inflammatory-associated apoptosis pathway that causes the retention of
469 embryos in the oviduct and prevents their timely transport to the uterus. However, the ovarian-
470 specific functions were found to be unaffected despite the loss of *Atg14* in the corpus luteum.

471 The human endometrium is a complex dynamic tissue that undergoes sequential
472 phases of proliferation and differentiation to support embryo implantation during the
473 conceptive. However, in the absence of an implanting embryo, the endometrium sheds
474 (menstruation) and initiates the regeneration process [40]. Previous reports indicated that
475 autophagy is modulated in the human endometrium during the menstrual cycle. For example,
476 autophagy is altered during the proliferative and secretory phases of the menstrual cycle with
477 its highest activity occurring during the secretory phase when the stroma is decidualized [41].
478 Similarly, the level of autophagy was higher in postmenopausal human uterine epithelial cells
479 compared to premenopausal uterine epithelial cells indicating the onset of autophagy upon
480 estrogen deprivation [42]. Although all these studies reported that autophagy is hormonally
481 regulated, however, the role of autophagy-specific proteins in the endometrium was not
482 established till our group's recent reports. Specifically, studies from our group reported the
483 role of three different autophagy-associated proteins: FIP200 [25], ATG16L [27], and BECLIN-
484 1 in uterine functions [26]. Conditional ablation of *Fip200* and *Atg16l* in the uterus displayed
485 fertility defects owing to impaired implantation, uterine receptivity, and decidualization defects.

486 On the contrary, loss of *Beclin1* in the uterus caused progressive loss of endometrial
487 progenitor stem cells resulting in severe uterine developmental defects and rendering the mice
488 infertile [26]. Although the autophagy-related proteins we studied so far influenced uterine
489 functions, [25-27], we found a distinct role for ATG14 in both the uterine and oviduct-specific
490 functions. It is intriguing to note that the absence of ATG14 did not affect the tissue integrity
491 of the uterus. However, the severe structural abnormalities in the oviduct due to *Atg14* ablation
492 unearthed a unique function of Atg14 in maintaining oviduct homeostasis. This distinctive role
493 of ATG14, unlike other autophagy proteins, might be due to its pivotal role in the assembly of
494 PtdIns3K complexes which is not the case for either FIP200 or ATG16L [40, 43, 44].
495 Nevertheless, understanding the specific contributions of each core autophagy protein in
496 reproductive tract functions is necessary which requires substantial efforts.

497 The retention of preimplantation embryos in the oviduct has been established as a
498 significant contributor to implantation failures, presenting challenges to the overall
499 reproductive health of women [8-10]. Embryo transport in the oviduct is known to be controlled
500 primarily by two major physiological responses: ciliary activity and muscle contractility. In our
501 study, a dramatic decrease in the number of Foxj1^{+ve} ciliary epithelial cells and Pax-8^{+ve}
502 secretory cells in *Atg14* cKO mice implied cell-type specific actions for ATG14 in the oviduct.
503 Interestingly, the specific ablation of *Atg14* in Foxj1+ve ciliary epithelial cells of the oviduct
504 does not appear to impact fertility. This suggests that the absence of ATG14 within ciliary cells
505 does not impact the process of embryo transport. Although unexpected, this is consistent with
506 other reports that have demonstrated the dispensability of cilia for embryo transport in the
507 oviduct [8, 9].

508 Pyroptosis is a highly inflammatory form of programmed cell death, characterized by
509 cell swelling, flattening of the cytoplasm, and large bubbles-like protrusions on the plasma
510 membrane [45-47]. Several recent studies found a link between autophagy and pyroptosis
511 [48]. *In vivo* studies also found that mice lacking the autophagy genes *Atg14*, *Fip200*, *Atg5*, or
512 *Atg7* in myeloid cells had more pronounced lung inflammation [49]. In our study, cellular
513 swelling, and fused membranous structures (a unique feature of activation of pyroptosis)

514 were observed in the oviductal epithelial folds from *Atg14* cKO mice. This aberrant activation
515 of the pyroptosis pathway due to loss of *Atg14* appears to adversely affect the oviduct cellular
516 structural integrity. These findings have implications beyond the oviduct, as autophagy can
517 modulate the inflammatory signaling pathway through different avenues. For example, first,
518 autophagy prevents mitochondrial reactive oxygen species release that can activate the
519 inflammasome by inhibiting IL1-β and IL18 production through the digestion of dysfunctional
520 mitochondria [50]. Second, autophagy is capable of targeting inflammasome complexes for
521 degradation, which prevents the cleavage of pro-IL-1β and pro-IL-18 into biologically active
522 forms. Finally, autophagy machinery further regulates IL-1β levels by engulfing and degrading
523 pro-IL-1β proteins [50]. In our study, accumulation of abnormally enlarged and dysfunctional
524 mitochondria in the absence of ATG14 in the oviduct clearly suggests the induction of severe
525 inflammatory conditions hampering the embryo transit through the oviduct. These findings are
526 further substantiated by the upregulation of pivotal mediators of the pyroptosis program,
527 including GSDMD and caspase-1, in *Atg14* cKO mice. Notably, the induction of pyroptosis in
528 the absence of ATG14 is specifically localized to the oviducts, with no parallel activation
529 detected in either the ovary or uterus. One potential reason for this observed phenomenon
530 could be the oviduct's unique molecular signatures that get activated in response to the
531 presence of gametes. A recent study by Finnerty et al. (2024) reported that sperm induce pro-
532 inflammatory conditions in the oviduct, which are preceded by an anti-inflammatory response
533 triggered by the presence of embryos [51]. The persistent activation of inflammatory or
534 pyroptotic conditions following the loss of Atg14 suggests that Atg14 may be a critical
535 autophagy protein responsible for suppressing pyroptosis in the oviduct. Moreover,
536 understanding the complex rheostat between the ATG14 and inflammation regulatory axis is
537 highly intriguing and will necessitate future studies employing sophisticated models, such as
538 combined knockout mice where ATG14 is deleted alongside key inflammatory regulators (e.g.,
539 NLRP3, GSDMD, or CASPASE-1).

540 In this report, we revealed tissue-specific roles of ATG14 in governing oviductal
541 transport, and uterine receptivity which are necessary for embryo implantation and pregnancy

542 establishment. Of mechanistic insights, we delineated a novel function of ATG14 as a negative
543 regulator of pyroptosis, which is vital for proper embryo transport in the oviduct (**Fig. 6F**). Thus,
544 this study not only sheds light on the involvement of autophagy in oviductal embryo transport
545 but also underscores the importance of autophagy in preserving the oviduct tissue integrity.
546 Such insights hold promise for advancing our understanding of gynecological pathologies
547 associated with the oviduct including tubal pregnancies.

548 **Acknowledgments**

549 We thank Goutham Davuluri, and Ashirbad Guria from our group for the technical assistance.
550 We thank Dr. Robert Lawrence (senior editor at Baylor College of Medicine) for assistance
551 with manuscript editing. We thank WashU Molecular Microbiology Imaging Facility for
552 assisting us with transmission electron microscopy. This work was funded, in part, by the
553 National Institutes of Health/National Institute of Child Health and Human Development
554 (grants R01HD102680, R01HD104813, and R01HD065435) to RK, R01 HD-042311 to JPL,
555 and in part by National Institutes of Health/National Heart, Lung, and Blood Institute (grant
556 R35HL145242) to MJH.

557 **Authors' roles**

558 PP and RK designed experiments, conducted most of the studies, analyzed the data, and
559 wrote the manuscript. AKO, VKM, and MNR conducted some of the experiments. MJH, JL,
560 SA, YZ, and KHM, provided critical reagents for the study. RM helped us with oviduct
561 pathology phenotype analysis. RK conceived the project, supervised the work, and wrote the
562 manuscript. All authors critically reviewed the manuscript.

563 **Conflict of Interest**

564 The authors have declared that no conflict of interest exists.

565 **Table 1**: **Six-month breeding trial of *Atg14* control and cKO females with wild-type males**

566 **Table 2**: **Six-month breeding trial of *Foxj1*/*Atg14* control and cKO females with wild-type**

567 **males**

568

Figure legends

Figure 1: *Atg14* loss in the FRT results in infertility. (**A**) Representative immunofluorescent images of uteri from pregnant mice (n=3) at the indicated days of pregnancy stained with an ATG14-specific antibody (green). LE: luminal epithelium, G: glands, S: stroma, Scale bar: 100 µm. Rabbit IgG was used as an isotype control for staining. (**B**) Relative transcript levels of *Atg14* mRNA in uteri from pregnant mice (n=3-5) at indicated days of pregnancy. mRNA levels are normalized to levels of 18S m-RNA. Data are presented as mean ±SEM; **P<0.01, P>0.05, ns=non-significant. (**C**) Relative mRNA levels of *Atg14* in 8-week-old virgin control and cKO mice uteri, ovary, and liver (n=5). mRNA levels are normalized to levels of 18S mRNA. Data are presented as mean ±SEM; ***P<0.001, P>0.05, ns=non-significant. (**D**) Representative immunofluorescent images of ATG14 expression in different uterine compartments in control (n=5) and *Atg14* cKO mice (n=5). LE: luminal epithelium, G: glands, S: stroma. (**E**) (*left panel*) Relative number of pups/female/litter and (*right panel*) and relative number of total pups/months of *Atg14* control (n=4) and cKO mice (n=5) sacrificed after the breeding trial. Data are presented as mean ±SEM; ***P<0.001; P>0.05, ns=non-significant.

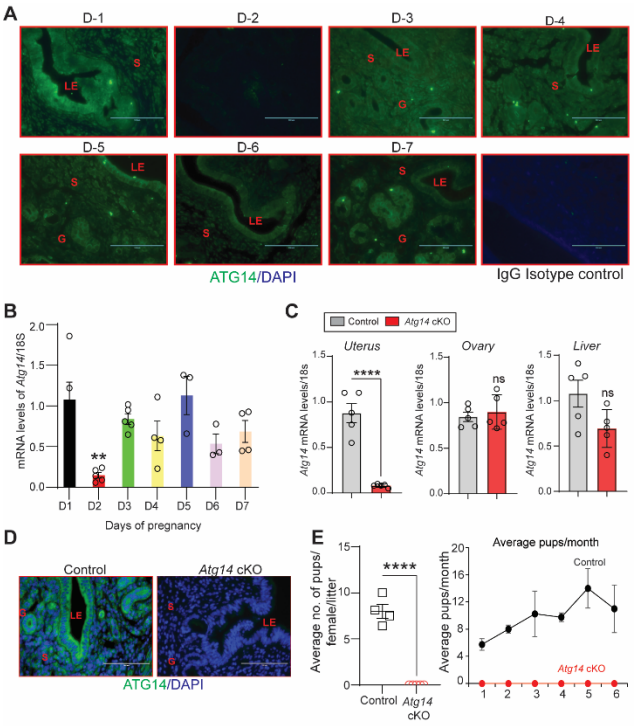

Figure 1

585 **Figure 2: *Atg14* is critical for embryo implantation, and uterine receptivity.** (**A**) Gross
586 images of 5.0 dpc uteri of control (n=5) and *Atg14* cKO mice (n=5) injected with Chicago Sky
587 Blue dye to visualize implantation sites (denoted by black arrows) (*left panel*). H&E-stained
588 cross-sections (6X & 20X) of 5.0 dpc uteri of control (n=5) and *Atg14* cKO (n=5) mice to
589 visualize embryo implantation (*Middle panel*). The asterisk denotes the embryo.
590 Immunofluorescence analysis of uterine tissues from control (n=5) and *Atg14* cKO mice (n=5),
591 stained with MUC1 and KRT8 (*right panel*). LE: luminal epithelium, G: glands, S: stroma. (**B**)
592 Representative immunofluorescence images of uteri from control (n=5) and *Atg14* cKO mice
593 (n=5) stained for Ki-67 following Oil or E2 or E2+P4 treatment (n=5 mice/group); scale bar:
594 100 µm. LE: luminal epithelium, G: glands, S: stroma. (**C**) Immunofluorescence analysis of
595 KRT8 (green), MUC1 (Red), and (**D**) Ki-67 (red) in the uteri of 4 dpc control and *Atg14* cKO
596 mice; scale bars, 100 µm. (**E**) Relative transcript levels of *Lif*, *Mcm2*, *Ccnd1,* and *Fgf18* in
597 control and cKO uteri at 4dpc. mRNA levels are normalized to levels of 18S m-RNA. Data are
598 presented as mean ±SEM; ns=non-significant. (**F**) Levels of steroid hormones estradiol and
599 progesterone from serum collected during euthanasia of 4 dpc control or cKO mice.

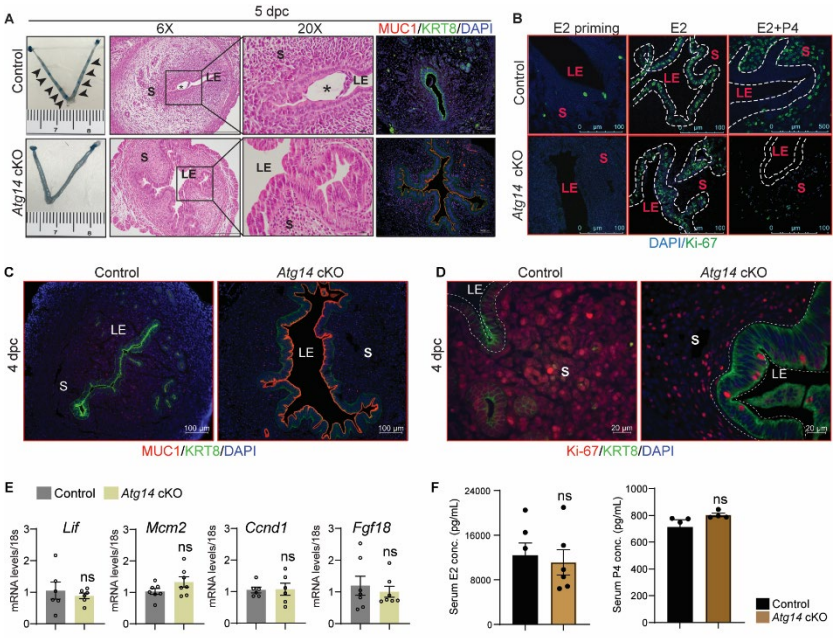

Figure 2

601 **Figure 3: *Atg14* is critical for embryo transport in oviduct.** (**A**) Representative images
602 (*upper panel*) and (**B**) Percentage of embryos (*lower panel*) collected at 4 dpc from the uteri
603 or the oviducts of control (n=6) or *Atg14* cKO mice (n=6-8). (**C**) Percentage of blastocysts,
604 morulae, developmentally delayed or nonviable embryos collected from *Atg14* control mice
605 uteri and Atg14 cKO mice oviducts at 4 dpc. (**D**) Histological analysis using H&E staining of
606 the ampullary and isthmic region of the oviduct from control and *Atg14* cKO female mice at 4
607 dpc (n=3 mice/genotype). (**E**) Embryos retrieved from the oviduct and uterus of super-ovulated
608 *Atg14* control or cKO mice at 4 dpc (n=3 mice/genotype). (**F**) Immunofluorescence analysis of
609 KRT8 (green), and α-SMA (Red), in the oviduct of 4 dpc control (n=5) and *Atg14* cKO mice
610 (n=5) ampulla (*upper panel*) and isthmus (*lower panel*).

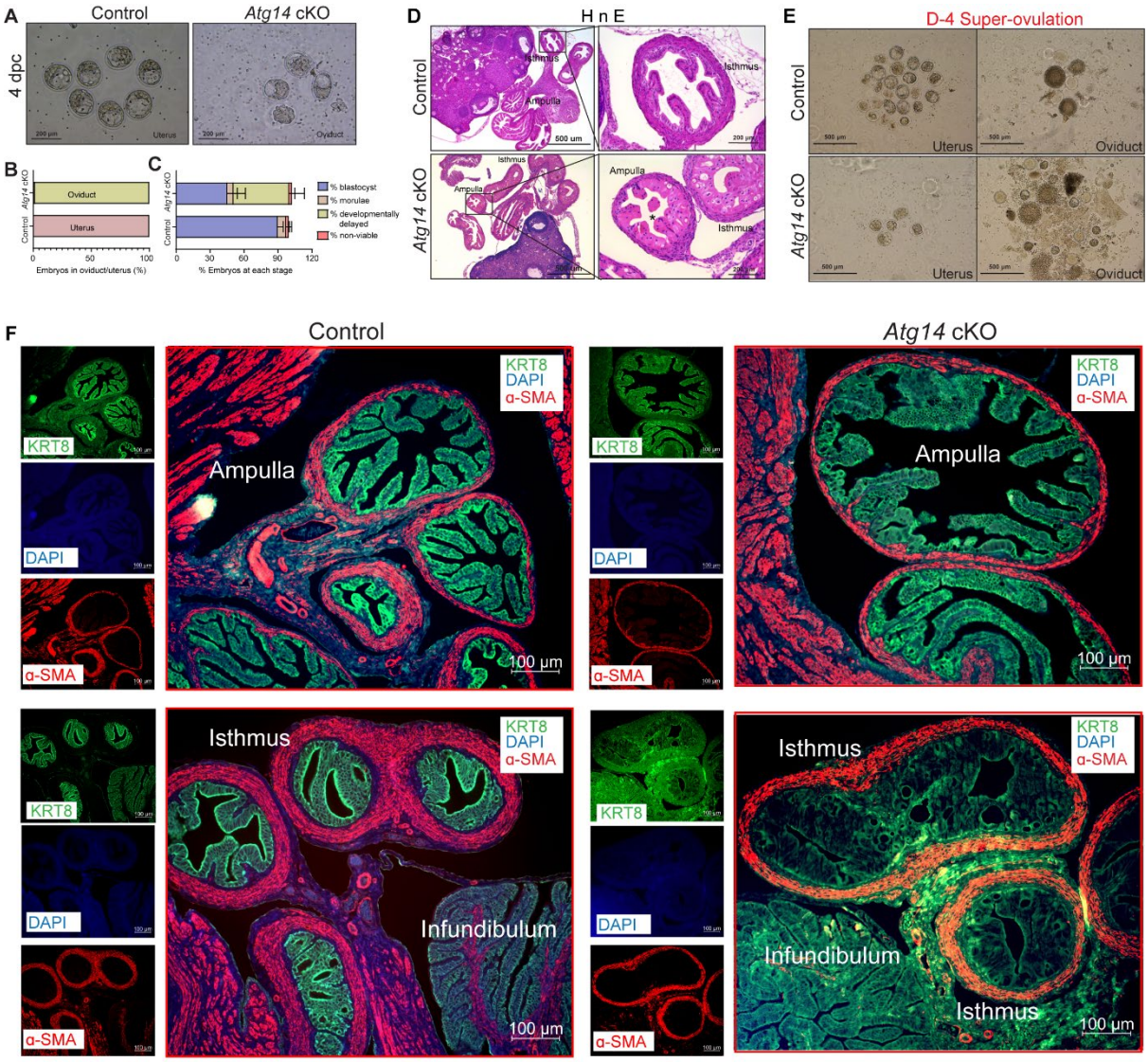

Figure 3

Figure 4: *Atg14* loss in oviduct cilia is dispensable for embryo transport. (A) Immunofluorescence analysis of acetylated α-tubulin (green), and DAPI (blue) in oviduct of 4 dpc control (n=5) and *Atg14* cKO mice (n=5). (**B**) Immunohistochemical analysis of FOXJ1 and PAX8 at 4 dpc (n=5). (**C**) Immunohistochemical analysis of acetylated α-tubulin in 8-week-old control (n=5) and *Foxj1*/*Atg14* cKO mice (n=5). Images are taken at 6X and 40X. Scale bar: 100μm and 10 μm. (**D & E**) Relative number of pups/females/litter and relative number of total pups/months of control (n=5) and *Foxj1*/*Atg14* cKO mice (n=5) sacrificed after the breeding trial. Data are presented as mean ± SEM; P>0.05, ns=non-significant. (**F**) Gross images of 5.0 dpc uteri of control (n=3) and *Foxj1/Atg14 cKO mice* (n=3) injected with Chicago Sky Blue dye to visualize implantation sites (denoted by black arrows).

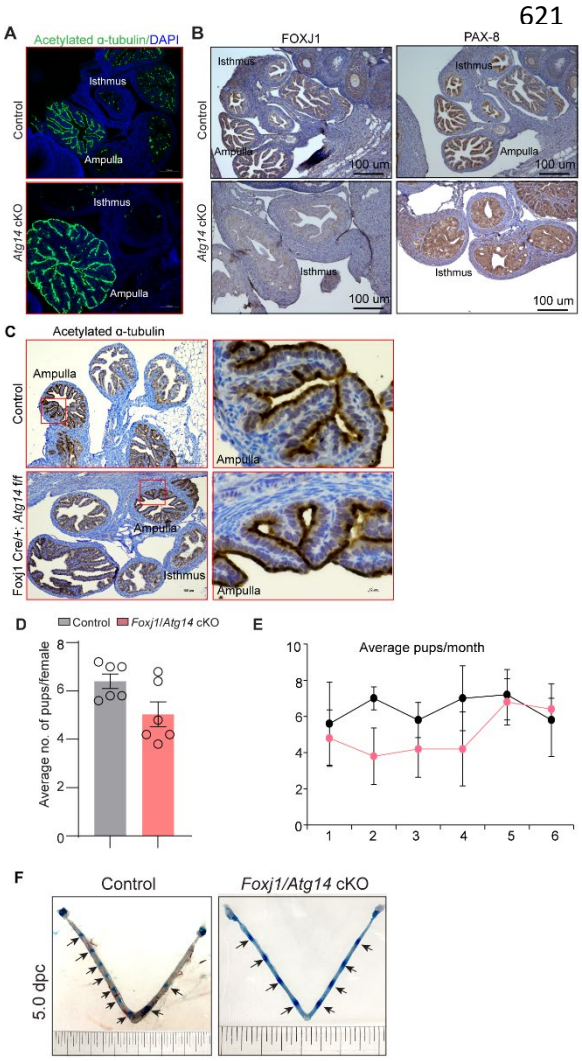

Figure 4

622 **Figure 5: *Atg14* facilitates embryo transport in the oviduct by preserving mitochondrial**
623 **integrity and inhibiting the activation of pyroptosis**. (**A**) Transmission electron microscopy
624 of oviducts at 4 dpc from control (n=3) and *Atg14* cKO (n=3)**.** Black arrowheads in control
625 oviducts show small, compact mitochondria with tight cristae. Red arrowheads in cKO oviducts
626 show abnormally enlarged mitochondria with loose cristae. (**B**) Immunofluorescence analysis
627 of TOM20 (green) and Cytochrome C (red) in *Atg14* control and cKO oviducts cryo-sections.
628 The inset shows the zoomed image of the selected area from control and cKO oviducts,
629 Arrowheads in the cKO inset oviduct section show the leaked cytochrome C in the cytoplasm.
630 Tissues were counterstained with DAPI (blue) to visualize nuclei; scale bars, 10 μm. (**C**)
631 Relative transcript levels of *Opa1*, *Cox4i2*, *Drp1,* and Pink1 in oviduct tissues. Data are
632 presented as mean ±SEM. *P<0.05; **P<0.01 compared with controls. 18S was used as an
633 internal control (**D**) Immunofluorescence analysis of GSDMD (red) + KRT8 (green), Caspase-
634 1 (red) + KRT8 (green) in oviducts of adult control (n=5), and *Atg14* cKO mice (n=5). Tissues
635 were counterstained with DAPI (blue) to visualize nuclei; scale bars, 100 μm. (**E**)
636 Immunohistochemical analysis of GSDMD expression in adult oviduct tissues (*left panel*). The
637 middle and -right panels show the zoom-in images to show the relative GSDMD expression in
638 the ampulla and isthmus section from control and cKO oviducts. (**F**) Immunohistochemical
639 analysis of GSDMD expression in adult uterus and ovary tissues (**G**) Western blotting to show
640 protein levels of Caspase-1, and GSDMD in oviduct tissues. β-actin is used as a loading
641 control. (**H**) Relative transcript levels of *Tnf-α* and *Cxcr3* in oviduct tissues. Data are presented
642 as mean ±SEM. *P<0.05; **P<0.01; ***P<0.001 compared with controls. 18S was used as an
643 internal control.

644

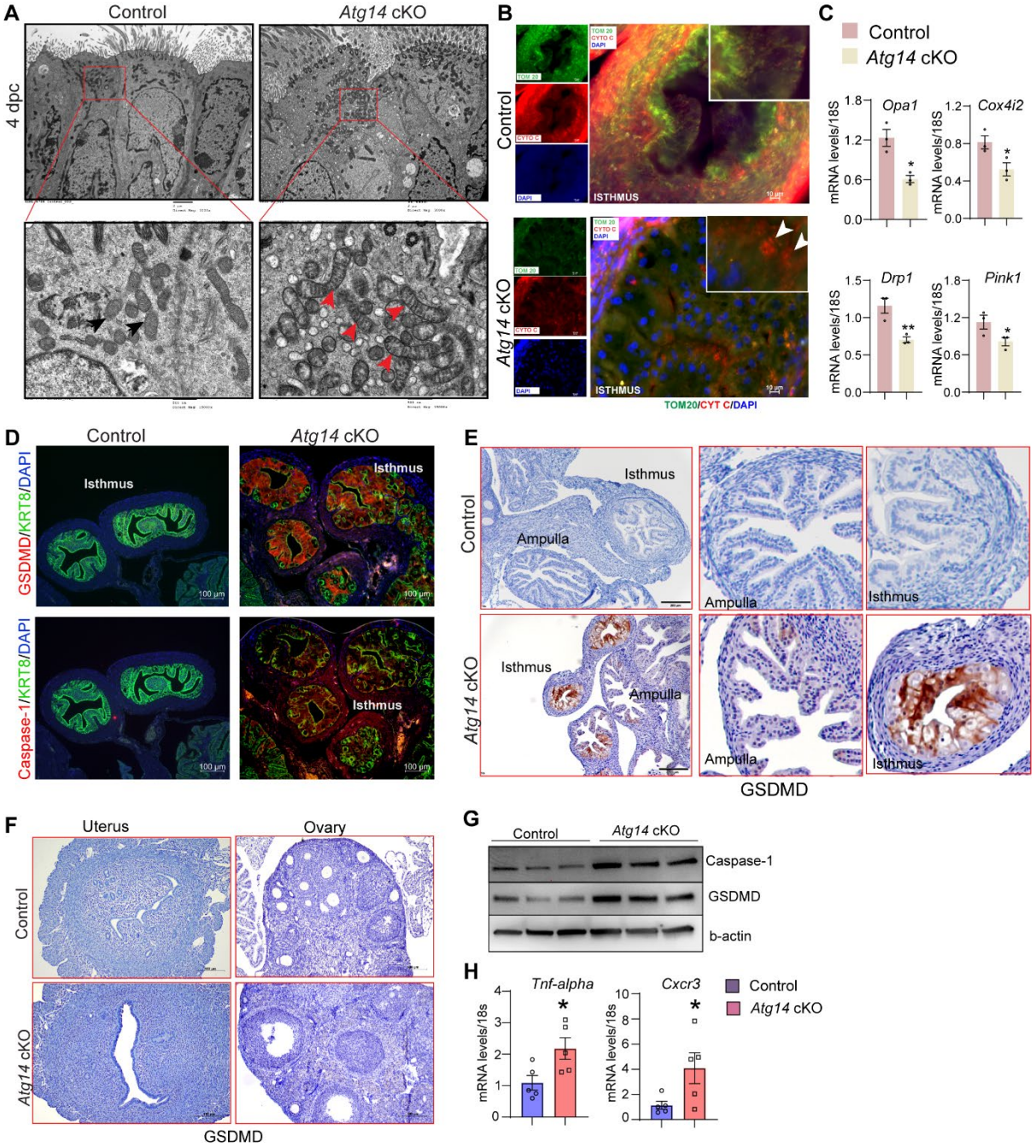
A
Control
Atg14 cKO
4 dpc
B
Control
Atg14 cKO
ISTHMUS
TOM20/CYT C/DAPI
C
Control
Atg14 cKO
Opa1
Cox4i2
Drp1
Pink1
mRNA levels/18S
D
Control
Atg14 cKO
GSDMD/KRT8/DAPI
Caspase-1/KRT8/DAPI
Isthmus
100 μm
E
Control
Atg14 cKO
Isthmus
Ampulla
GSDMD
F
Uterus
Ovary
Control
Atg14 cKO
GSDMD
G
Control
Atg14 cKO
Caspase-1
GSDMD
b-actin
H
Tnf-alpha
Cxcr3
mRNA levels/18s
Control
Atg14 cKO

Figure 5

Figure 6: Pharmacological activation of pyroptosis in the oviduct inhibits embryo transport. (**A**) Experimental strategy for pyroptosis activation in pregnant female mice (**B**) Embryos flushed from the vehicle (n=3) or polyphyllin VI treated (n=3) D-4 pregnant females. (**C**) Percentage of embryos recovered from oviducts or uteri. (**D**) Percentage of blastocysts, morulae, developmentally delayed or nonviable embryos collected from vehicle uteri or Polyphyllin IV oviducts at 4 dpc. (**E**) Immunohistochemistry to show GSDMD expression in the isthmus section of polyphyllin IV-treated and vehicle-treated mice. 40X objective, Scale bar: 5 µm. (**F**) Graphical illustration to show embryo transport and pyroptosis regulation in the oviduct.

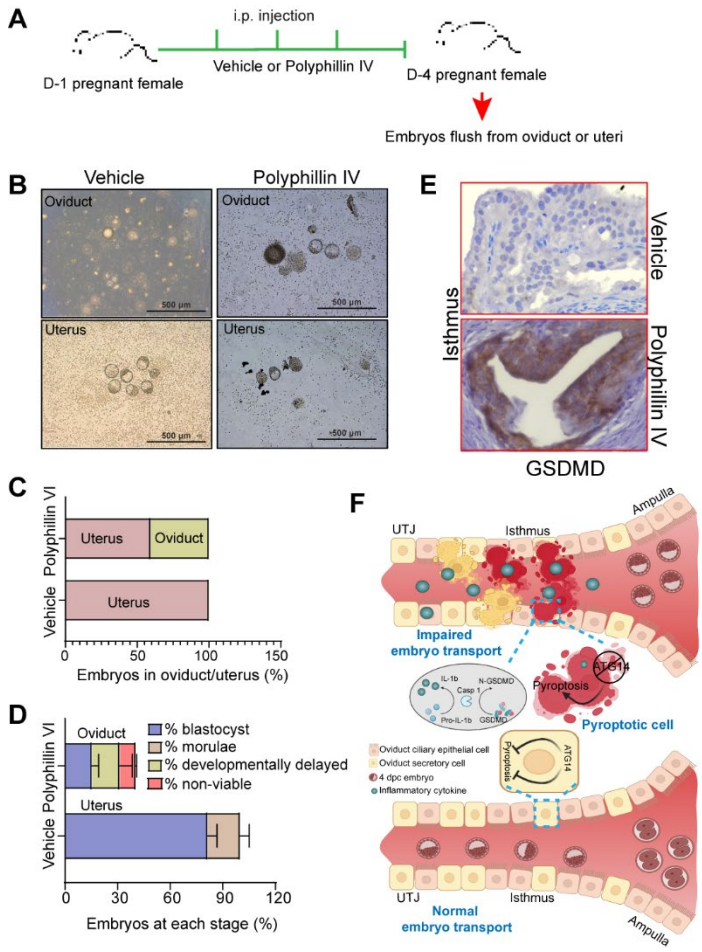

Figure 6

656 **References**

657

658 1. Wang, H. and S.K. Dey, *Roadmap to embryo implantation: clues from mouse models.* Nat Rev
659 Genet, 2006. **7**(3): p. 185-99.
660 2. Ford, M.J., et al., *Oviduct epithelial cells constitute two developmentally distinct lineages that*
661 *are spatially separated along the distal-proximal axis.* Cell Rep, 2021. **36**(10): p. 109677.
662 3. McKey, J., et al., *Integration of mouse ovary morphogenesis with developmental dynamics of*
663 *the oviduct, ovarian ligaments, and rete ovarii.* Elife, 2022. **11**.
664 4. Harwalkar, K., et al., *Anatomical and cellular heterogeneity in the mouse oviduct-its potential*
665 *roles in reproduction and preimplantation developmentdagger.* Biol Reprod, 2021. **104**(6): p.
666 1249-1261.
667 5. Dirksen, E.R. and P. Satir, *Ciliary activity in the mouse oviduct as studied by transmission and*
668 *scanning electron microscopy.* Tissue Cell, 1972. **4**(3): p. 389-403.
669 6. Li, S., et al., *Estrogen receptor alpha is required for oviductal transport of embryos.* FASEB J,
670 2017. **31**(4): p. 1595-1607.
671 7. Jiang, R., et al., *CDC42 governs normal oviduct multiciliogenesis through activating AKT to*
672 *ensure timely embryo transport.* Cell Death Dis, 2022. **13**(9): p. 757.
673 8. Herrera, G.G.B., et al., *Oviductal Retention of Embryos in Female Mice Lacking Estrogen*
674 *Receptor alpha in the Isthmus and the Uterus.* Endocrinology, 2020. **161**(2).
675 9. Wang, H., et al., *Aberrant cannabinoid signaling impairs oviductal transport of embryos.* Nat
676 Med, 2004. **10**(10): p. 1074-80.
677 10. Qian, J., et al., *Caffeine consumption during early pregnancy impairs oviductal embryo*
678 *transport, embryonic development and uterine receptivity in mice.* Biol Reprod, 2018. **99**(6): p.
679 1266-1275.
680 11. Klionsky, D.J., *Autophagy: from phenomenology to molecular understanding in less than a*
681 *decade.* Nat Rev Mol Cell Biol, 2007. **8**(11): p. 931-7.
682 12. Wen, X. and D.J. Klionsky, *An overview of macroautophagy in yeast.* J Mol Biol, 2016. **428**(9 Pt
683 A): p. 1681-99.
684 13. Itakura, E., et al., *Beclin 1 forms two distinct phosphatidylinositol 3-kinase complexes with*
685 *mammalian Atg14 and UVRAG.* Mol Biol Cell, 2008. **19**(12): p. 5360-72.
686 14. Sun, Q., et al., *Identification of Barkor as a mammalian autophagy-specific factor for Beclin 1*
687 *and class III phosphatidylinositol 3-kinase.* Proc Natl Acad Sci U S A, 2008. **105**(49): p. 19211-
688 6.
689 15. Wang, Y.Y., X.L. Liu, and R. Zhao, *Induction of Pyroptosis and Its Implications in Cancer*
690 *Management.* Front Oncol, 2019. **9**: p. 971.
691 16. Man, S.M., R. Karki, and T.D. Kanneganti, *Molecular mechanisms and functions of pyroptosis,*
692 *inflammatory caspases and inflammasomes in infectious diseases.* Immunol Rev, 2017. **277**(1):
693 p. 61-75.
694 17. Wei, X., et al., *Role of pyroptosis in inflammation and cancer.* Cell Mol Immunol, 2022. **19**(9):
695 p. 971-992.
696 18. Lin, L., et al., *Autophagy, Pyroptosis, and Ferroptosis: New Regulatory Mechanisms for*
697 *Atherosclerosis.* Front Cell Dev Biol, 2021. **9**: p. 809955.
698 19. Li, X., et al., *Autophagy, Pyroptosis and Ferroptosis are Rising Stars in the Pathogenesis of*
699 *Diabetic Nephropathy.* Diabetes Metab Syndr Obes, 2024. **17**: p. 1289-1299.
700 20. Zhao, H., et al., *The Role of Autophagy and Pyroptosis in Liver Disorders.* Int J Mol Sci, 2022.
701 **23**(11).
702 21. Kong, Y., et al., *The Natural Flavonoid Galangin Elicits Apoptosis, Pyroptosis, and Autophagy*
703 *in Glioblastoma.* Front Oncol, 2019. **9**: p. 942.
704 22. Kim, J.Y., et al., *Streptococcus pneumoniae induces pyroptosis through the regulation of*
705 *autophagy in murine microglia.* Oncotarget, 2015. **6**(42): p. 44161-78.

23. Song, Z.H., et al., *Germ cell-specific Atg7 knockout results in primary ovarian insufficiency in female mice.* Cell Death Dis, 2015. **6**(1): p. e1589.
24. Gawriluk, T.R., et al., *Beclin-1 deficiency in the murine ovary results in the reduction of progesterone production to promote preterm labor.* Proc Natl Acad Sci U S A, 2014. **111**(40): p. E4194-203.
25. Oestreich, A.K., et al., *The autophagy protein, FIP200 (RB1CC1) mediates progesterone responses governing uterine receptivity and decidualizationdagger.* Biol Reprod, 2020. **102**(4): p. 843-851.
26. Popli, P., et al., *Beclin-1-dependent autophagy, but not apoptosis, is critical for stem-cell-mediated endometrial programming and the establishment of pregnancy.* Dev Cell, 2023. **58**(10): p. 885-897 e4.
27. Oestreich, A.K., et al., *The Autophagy Gene Atg16L1 is Necessary for Endometrial Decidualization.* Endocrinology, 2020. **161**(1).
28. Matsunaga, K., et al., *Two Beclin 1-binding proteins, Atg14L and Rubicon, reciprocally regulate autophagy at different stages.* Nat Cell Biol, 2009. **11**(4): p. 385-96.
29. Soyal, S.M., et al., *Cre-mediated recombination in cell lineages that express the progesterone receptor.* Genesis, 2005. **41**(2): p. 58-66.
30. Zhang, Y., et al., *A transgenic FOXJ1-Cre system for gene inactivation in ciliated epithelial cells.* Am J Respir Cell Mol Biol, 2007. **36**(5): p. 515-9.
31. Chadchan, S.B., et al., *Antibiotic therapy with metronidazole reduces endometriosis disease progression in mice: a potential role for gut microbiota.* Hum Reprod, 2019. **34**(6): p. 1106-1116.
32. Chojnacki, A.K., et al., *Tissue imaging reveals disruption of epithelial mitochondrial networks and loss of mitochondria-associated cytochrome-C in inflamed human and murine colon.* Mitochondrion, 2023. **68**: p. 44-59.
33. Kommagani, R., et al., *The Promyelocytic Leukemia Zinc Finger Transcription Factor Is Critical for Human Endometrial Stromal Cell Decidualization.* PLoS Genet, 2016. **12**(4): p. e1005937.
34. Teng, J.F., et al., *Polyphyllin VI Induces Caspase-1-Mediated Pyroptosis via the Induction of ROS/NF-kappaB/NLRP3/GSDMD Signal Axis in Non-Small Cell Lung Cancer.* Cancers (Basel), 2020. **12**(1).
35. Tong, W. and J.W. Pollard, *Progesterone inhibits estrogen-induced cyclin D1 and cdk4 nuclear translocation, cyclin E- and cyclin A-cdk2 kinase activation, and cell proliferation in uterine epithelial cells in mice.* Mol Cell Biol, 1999. **19**(3): p. 2251-64.
36. Ito, S., Y. Yamamoto, and K. Kimura, *Analysis of ciliogenesis process in the bovine oviduct based on immunohistochemical classification.* Mol Biol Rep, 2020. **47**(2): p. 1003-1012.
37. Liu, Q., et al., *The role of mitochondria in NLRP3 inflammasome activation.* Mol Immunol, 2018. **103**: p. 115-124.
38. Shi, Y., et al., *Echinacoside Induces Mitochondria-Mediated Pyroptosis through Raf/MEK/ERK Signaling in Non-Small Cell Lung Cancer Cells.* J Immunol Res, 2022. **2022**: p. 3351268.
39. Wang, Y., et al., *Mitochondrial ROS promote macrophage pyroptosis by inducing GSDMD oxidation.* J Mol Cell Biol, 2019. **11**(12): p. 1069-1082.
40. Popli, P., A.J. Sun, and R. Kommagani, *The Multifaceted Role of Autophagy in Endometrium Homeostasis and Disease.* Reprod Sci, 2022. **29**(4): p. 1054-1067.
41. Choi, J., et al., *Differential induction of autophagy by mTOR is associated with abnormal apoptosis in ovarian endometriotic cysts.* Mol Hum Reprod, 2014. **20**(4): p. 309-17.
42. Zhou, S., et al., *Author Correction: Menopause-induced uterine epithelium atrophy results from arachidonic acid/prostaglandin E2 axis inhibition-mediated autophagic cell death.* Sci Rep, 2020. **10**(1): p. 6915.
43. Fan, W., A. Nassiri, and Q. Zhong, *Autophagosome targeting and membrane curvature sensing by Barkor/Atg14(L).* Proc Natl Acad Sci U S A, 2011. **108**(19): p. 7769-74.

44. Diao, J., et al., *ATG14 promotes membrane tethering and fusion of autophagosomes to endolysosomes.* Nature, 2015. **520**(7548): p. 563-6.
45. Ma, X., et al., *LPS Mediates Bovine Endometrial Epithelial Cell Pyroptosis Directly Through Both NLRP3 Classical and Non-Classical Inflammasome Pathways.* Front Immunol, 2021. **12**: p. 676088.
46. Cookson, B.T. and M.A. Brennan, *Pro-inflammatory programmed cell death.* Trends Microbiol, 2001. **9**(3): p. 113-4.
47. Jorgensen, I. and E.A. Miao, *Pyroptotic cell death defends against intracellular pathogens.* Immunol Rev, 2015. **265**(1): p. 130-42.
48. Liu, J., et al., *Autophagy blockage promotes the pyroptosis of ox-LDL-treated macrophages by modulating the p62/Nrf2/ARE axis.* J Physiol Biochem, 2021. **77**(3): p. 419-429.
49. Lu, Q., et al., *Homeostatic Control of Innate Lung Inflammation by Vici Syndrome Gene Epg5 and Additional Autophagy Genes Promotes Influenza Pathogenesis.* Cell Host Microbe, 2016. **19**(1): p. 102-13.
50. Netea-Maier, R.T., et al., *Modulation of inflammation by autophagy: Consequences for human disease.* Autophagy, 2016. **12**(2): p. 245-60.
51. Finnerty, R.M., et al., *Multi-omics analyses and machine learning prediction of oviductal responses in the presence of gametes and embryos.* bioRxiv, 2024.